

**Numerical simulations of elastic-plastic Richtmyer-Meshkov instability of multiple interfaces**Xiangyi Liu , Fenghui Lin , Zhiye Zhao, Nansheng Liu \*, and Xiyun Lu *Department of Modern Mechanics, University of Science and Technology of China, Hefei, Anhui 230026, China*

(Received 10 November 2023; accepted 19 February 2024; published 11 March 2024)

The elastic-plastic Richtmyer-Meshkov instability of multiple interfaces is investigated by numerical simulation using a multimaterial solid mechanics algorithm based on an Eulerian framework. This Richtmyer-Meshkov instability problem is realized by a copper layer that is flanked by vacuum and a copper block of different material strength. The research efforts are directed to reveal the influence of the layer thickness and material strength on the deformation of the perturbed solid-vacuum interface impacted by an initial shock. By varying the initial thickness ( $x_1$ ) of the copper layer and the yield stress ( $\sigma_{Y2}$ ) of the copper block, two deformation modes, which have been identified as the broken mode and the stable mode, are closely scrutinized. For a fixed  $x_1$  and a decreasing  $\sigma_{Y2}$ , the reflected rarefaction waves (RRWs), developing after the initial shock impacts the perturbed interface 1 (I1) between vacuum and the copper layer, become stronger after traveling across the interface 2 (I2). Subsequently, the velocity of I2 becomes larger, causing the width of I1 to grow larger. This width growth of I1 leads to a final separation of the spike from I1 and, consequently, the deformation mode changes from the stable mode to the broken mode. For a fixed  $\sigma_{Y2}$  and a decreasing  $x_1$ , the RRWs impact I2 at an earlier moment with a greater strength and thus the deformation mode changes from the stable mode to the broken mode. Meanwhile, the comparison of the spike width of cases whose deformation mode is the broken mode shows that there exists a maximum value of rescaled spike width, at which the deformation mode changes from the stable mode to the broken mode.

DOI: [10.1103/PhysRevE.109.035102](https://doi.org/10.1103/PhysRevE.109.035102)**I. INTRODUCTION**

The Richtmyer-Meshkov instability (RMI), named after the seminal work of Richtmyer [1] and Meshkov [2], arises when a shock wave interacts with a perturbed interface between two materials of different properties. Specifically, the misalignment between directions of the local density gradient across the interface (normal to the interface) and the shock pressure gradient (normal to the shock) produces a baroclinic deposition of vorticity on the interface. Consequently, this interaction leads to the unbounded growth of the perturbed interface unless a mechanism could dissipate or advect such vorticity. This instability can also occur in free surfaces separating continuous media from vacuum and it is regarded as the limiting case of a free-slip interface separating a solid or fluid material from a very rarified gas [3]. In the case in which Atwood number  $A = -1$ , the initial shockwave is driven through the material into the perturbed free surface. When the shockwave arrives at the free surface, it first releases to zero pressure at the perturbation minima and then reflects back into the material as a rarefaction wave. A short time later, the shockwave releases to zero pressure at the perturbation maxima, also reflecting back into the material as a rarefaction wave. Under these conditions, the stresses produced by the shockwave interaction with the perturbations cause the perturbation minima to compress, invert, and then grow in tension as RM instabilities (spikes) into vacuum. Because the compressed RM spikes grow quickly relative to the initial perturbation maxima, the initial maxima invert and form bubbles

that unstably grow into the material, causing the material to flow into the spikes to support the spike growth [4]. Although the RMI is originally regarded as the impulsive limit of the Rayleigh-Taylor instability [5,6], it has become increasingly important because it controls a variety of processes in nature and technology, such as inertial confinement fusion (ICF) [7] and astrophysical problems [8].

The canonical RMI, consisting of a single planar shock-wave interacting with a single corrugated interface separating two fluids, has been widely studied by numerical simulation, experimental research, and theoretical analysis [9–11]. As for the RMI involving the interaction between shock and multiple interfaces, which is a setup relevant to ICF and supernova collapse, most of the research has focused on gas curtains. For example, Refs. [12–15] consider a thin layer of fluid within another fluid. Hence, the multiple-interface RMI has been extensively investigated from the fluid dynamics perspective. However, this intriguing instability also appears in problems of interest in solid mechanics, for example, purely elastic and elastic-plastic RMIs. The research work of purely elastic RMI flow has been performed based on the analytical model [16] and linearized analysis [17], and the results show that the interface is always stable because the vorticity deposited on the material interface during the shock passing through is propagated away by the shear waves. On the other hand, the study of the RMI in elastic-plastic material primarily relies on numerical approaches other than purely analytical models since the plasticity theory is nonlinear and thus inaccessibly complicated.

The first research to describe the evolution of small perturbations at the solid-vacuum interface in the elastic-plastic

\*lns@ustc.edu.cn

RMI problem was conducted by Piriz *et al.* [18]. They developed an analytical model by using the relatively simple method which was presented in Ref. [16] to describe the behavior of the elastic medium. They found a relation among the long-term interface amplitude, the initial interface amplitude and growth rate, the unstressed density of material, and the yield stress of the material. A set of two-dimensional (2D) numerical simulations was also performed and the results agree very well with the analytical relation. Since then, the investigations of elastic-plastic RMI have been mainly focused on the long-term behavior of the interface, devoted to establishing a relationship between the parameters of long-term behavior and initial condition, and to inferring the yield stress of the material which is under complicated loading.

Specifically, Dimonte *et al.* [19] developed a model similar to that described in Ref. [18] at the metal-gas interface for the strength suppression of the RMI. This model can be used to infer the yield stress ( $\sigma_Y$ ) of copper in an explosively driven experiment and the results agree with previous ones obtained in Ref. [20]. By simulating the solid-vacuum RMI problem with perfect plastic constitutive, Ortega *et al.* [3] obtained an empirical law that presents a combined relation for the long-term perturbation amplitude of the interface, its maximum growth rate, the initial density, and the yield stress of the material. Moreover, this empirical law was extended to materials that follow more complex plastic behavior. Jensen *et al.* [21] performed RMI growth experiments using the free-surface configuration and estimated the tensile yield stress for cerium following a high-pressure, shock-induced phase transition by three methods. Two of the methods are based on the model developed by Dimonte *et al.* [19] and the yield stress values obtained using these three different methods were in reasonable agreement. Furthermore, the other improved models for the elastic-plastic RMI were also proposed to evaluate the material strength of solids under high pressures in previous experiments [4,22–25].

As mentioned above, most investigations of elastic-plastic RMI are focused on the long-term behavior of the interface, while little research has focused on the wave motion occurring before interface deformation, which is known to have an intriguing influence on the RMI dynamics. To this end, Liu *et al.* [26] have carried out comprehensive numerical simulations to systematically examine the behavior of the whole process of the solid-vacuum RMI at different initial perturbed interface amplitudes and yield stresses. They had documented three typical deformation modes for this RMI problem, namely, the broken mode, the stable mode, and the oscillating mode. In order to gain mechanistic insight into these three modes, the wave motions at the early stage, the subsequent interface deformation, and the temporal variations of interface positions and velocities were closely examined. Inspired by this work, in the present paper we consider the elastic-plastic RMI of multiple interfaces realized by a copper layer that is flanked by vacuum and a copper block of different material strength, and the main goal is to explore a full view on this interesting RMI problem which is closer to the setup relevant to ICF and supernova collapse.

In this study, the planar elastic-plastic RMI problem of multiple interfaces is systematically examined at different initial thicknesses of the copper layer and yield stresses of

the copper block. We find that two typical deformation modes appear, namely, the broken mode and the stable mode, when the initial thickness and the yield stress are varied. To clarify the differences of these two modes, the wave motions at the early stage, the subsequent interface deformation, and the temporal variations of interface positions and velocities are discussed in detail. Moreover, a maximum value of rescaled spike width is found as the critical value for the transition from the stable mode to the broken mode. The remainder of this paper is organized as follows. The numerical implementation and equations are briefly described in Sec. II. The problem description and validation of the simulation program are presented in Sec. III. The simulation results and discussions are exposed in Sec. IV. Finally, concluding remarks are summarized in Sec. V.

## II. GOVERNING EQUATIONS AND NUMERICAL IMPLEMENTATION

In the simulation of the elastic-plastic RMI problems, the equations of motion for the elastic-plastic solid materials are used in an Eulerian framework which is based on the work of Barton *et al.* [27,28]. In a fixed Cartesian frame of reference  $(x_1, x_2, x_3)$ , the equations of motion, which include the mass, momentum, energy, and deformation equations in differential form, are described as follows:

$$\frac{\partial \rho}{\partial t} + \frac{\partial \rho u_k}{\partial x_k} = 0, \quad (1a)$$

$$\frac{\partial \rho u_i}{\partial t} + \frac{\partial (\rho u_i u_k - \sigma_{ik})}{\partial x_k} = 0, \quad (1b)$$

$$\frac{\partial \rho (e + u_k u_k / 2)}{\partial t} + \frac{\partial [\rho u_k (e + u_k u_k / 2) - u_i \sigma_{ik}]}{\partial x_k} = 0, \quad (1c)$$

$$\frac{\partial \rho F_{ij}}{\partial t} + \frac{\partial (\rho F_{ij} u_k - \rho F_{kj} u_i)}{\partial x_k} = -u_i \frac{\partial \rho F_{kj}}{\partial x_k} - \varphi_{ij}, \quad (1d)$$

for  $i, j, k = 1, 2, 3$  denoting the coordinates and Einstein index notation being employed throughout this article.  $u_i$  is the component of velocity  $\mathbf{u}$ ,  $\sigma_{ij}$  is the component of stress tensor  $\boldsymbol{\sigma}$ , and  $e(\rho, S)$  is the inner energy with  $\rho$  being the density and  $S$  the entropy of the solid material. The elastic deformation gradient  $F_{ij} = \partial x_i / \partial X_j$  is used to measure relative displacements between particles where  $x_i$  and  $X_j$  denote the spatial and material coordinates, respectively. Hence, the density  $\rho$  varies according to

$$\rho = \frac{\rho_0}{|\mathbf{F}|}, \quad (2)$$

where  $\rho_0$  is the density of the initial unstressed solid and  $|\mathbf{F}|$  denotes the determinant of the elastic deformation gradient tensor. For the problem of two-dimensional deformations ( $F_{13} = F_{23} = F_{31} = F_{32} = 0$ ) considered here, the evolution equations [Eq. (1d)] of the elastic deformation gradient tensor  $\mathbf{F}$  are reduced to have four nontrivial components as  $F_{33}$  can be obtained from Eq. (2). The second term on the right-hand side of Eq. (1d), which represents the influence of the plasticity on the elastic deformations, is given by

$$\varphi_{ij} = \frac{1}{2\mu\tau} \sigma'_{ik} \rho F_{kj}, \quad (3)$$

TABLE I. Parameters for copper.

Parameter	Copper	Units
$\rho_0$	8.93	g/cm <sup>3</sup>
$K$	$15.28 \times 10^6$	m <sup>2</sup> /s <sup>2</sup>
$c_V$	$3.9 \times 10^2$	J/(kgK)
$T_0$	298	K
$\mu_0$	39.38	GPa
$\alpha$	1	—
$\beta$	3	—
$\gamma$	2	—

where  $\sigma'_{ik} = \sigma_{ik} - \sigma_{mm}\delta_{ik}/3$  is the tensor of deviatoric stress,  $\delta_{ik}$  is the Kronecker delta, and  $\mu$  is the shear modulus. Based on the previous treatment [28], the expression of relaxation time  $\tau$  takes the form

$$\tau = \tau_0 \left( \frac{\sigma_0}{\sigma_e} \right)^{m_1}, \quad \sigma_e = \sqrt{\frac{3}{2} \sigma'_{ij} \sigma'_{ij}}, \quad (4)$$

where  $\tau_0$  is a reference relaxation time,  $\sigma_0$  is the characteristic stress, and the exponent  $m_1$  controls the extent of rate dependence. This expression can be simplified to perfect plasticity in our simulations by setting  $\sigma_0 = \sigma_Y$ , and  $m_1$  high enough so that the equivalent stress  $\sigma_e$  conforms to the yield surface defined by  $\sigma_Y$  almost immediately.

A hyperelastic constitutive law [29,30], in which the stress state is acquired via direct differentiation of the equation of state (EOS) for the inner energy in consistency with the energy conservation equation, is used as follows:

$$\sigma_{ij} = \rho F_{ik} \frac{\partial e}{\partial F_{jk}}. \quad (5)$$

The Godunov-Romenski hyperelastic EOS [3,31] is employed for the modeling of elastic-plastic solids which considers contributions to the inner energy related to shear and hydrostatic deformations, respectively,

$$e = e_s + e_h, \quad (6a)$$

$$e_s = 2c_s^2(\rho)I^2, \quad I^2 = \frac{(I_1^H)^2}{3} - I_2^H, \quad (6b)$$

$$e_h = \frac{K}{2\alpha^2} \left[ \left( \frac{\rho}{\rho_0} \right)^\alpha - 1 \right]^2 + c_V T_0 \left( \frac{\rho}{\rho_0} \right)^\gamma \left[ \exp\left( \frac{S}{c_V} \right) - 1 \right], \quad (6c)$$

where  $c_s^2(\rho) = \mu/\rho = \mu_0\rho^\beta/\rho_0^{\beta+1}$ , and  $I_1^H, I_2^H$  are the first two invariants of the elastic Hencky strain tensor  $\mathbf{H} = \frac{1}{2} \ln(\mathbf{FF}^T)$ .  $\mu_0$  is the reference shear modulus,  $K$  is the squared bulk speed of sound,  $c_V$  is the heat capacity at constant volume,  $T_0$  is the reference temperature, and  $\alpha, \beta, \gamma$  are constant values. The material considered in this work is copper and the parameters, from Ref. [31], are listed in Table I.

Based on the previous work of Barton *et al.* [28], the numerical discretization of the motion equations of solid and the computation of the plasticity models are briefly described here. Specifically, the equations of motion for elastic-plastic solids are solved by using the Eulerian finite-difference

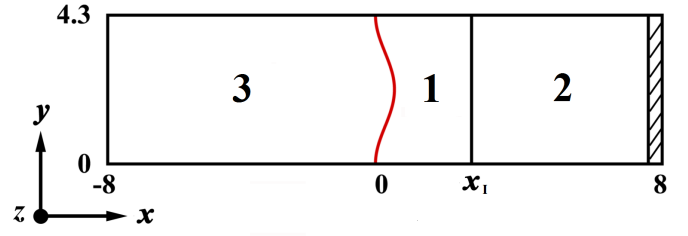


FIG. 1. Schematic of computational setup used for the elastic-plastic RMI of the considered multiple interfaces.

method in a fixed Cartesian grid. The state variables are stored at cell centers and the cell face numerical fluxes are formed through polynomial reconstruction of cell center variables by using a third-order, weighted, essentially nonoscillatory (WENO) method [32]. The time integration is approximated by using a third-order total variation diminishing Runge-Kutta method [33]. The plastic update can be reduced to a stiff ordinary differential equation dependent only on the local stress state and the solution for this ordinary differential equation can be simplified by using the hyperelastic EOS (6) and the perfect plastic model [28]. Sharp interface resolution is achieved by employing level-set functions to track the motions of the free surface between solid and vacuum and the slip surface between two solids [28], along with the modified ghost material method [34] to capture the necessary internal boundary conditions for material interactions. The necessary parameters used in the modified ghost material method, such as the density  $\rho$ , the velocity  $\mathbf{u}$ , the total energy  $E$ , and the elastic deformation gradient tensor  $\mathbf{F}$ , are obtained by solving the solid-vacuum or solid-solid one-dimensional Riemann problems along the normal direction of the interface via the Harten-Lax-van Leer discontinuities (HLLD) method [35].

### III. PROBLEM DESCRIPTION AND VALIDATION

#### A. Problem description

As shown by the schematic in Fig. 1, the problem to be considered is the two-dimensional planar elastic-plastic RMI, which contains a finite-thickness layer of copper (area 1) between the vacuum (area 3) and a copper block of different material strength (area 2). The rectangular computational domain extends from  $x \sim -8-8$  cm and  $y \sim 0-4.3$  cm, corresponding to a length of 16 cm and a width of 4.3 cm in the  $x$  and  $y$  directions, respectively. The computational domain is divided into three parts by two interfaces. The interface 1 (I1), plotted as a red line in Fig. 1, is perturbed with a sinusoidal wave  $x = -\xi_0 \cos(ky)$ , with  $k$  chosen in a way such that one wave cycle is included in the  $y$ -direction computational domain and the wavelength  $\lambda = 4.3$  cm. The vacuum is on the left side of I1 (area 3) and copper whose parameters are set in Table I is set to be on the rest of the simulation domain (areas 1 and 2). The copper is divided into two parts by the interface 2 (I2) at  $x = x_1$  cm, and these two parts are considered as multimaterials as they are set to have different material strength, namely, different yield stresses. The initial horizontal velocities of unstressed copper in areas 1 and 2 are set as 5 and 0 km/s, respectively, and the vertical velocities as

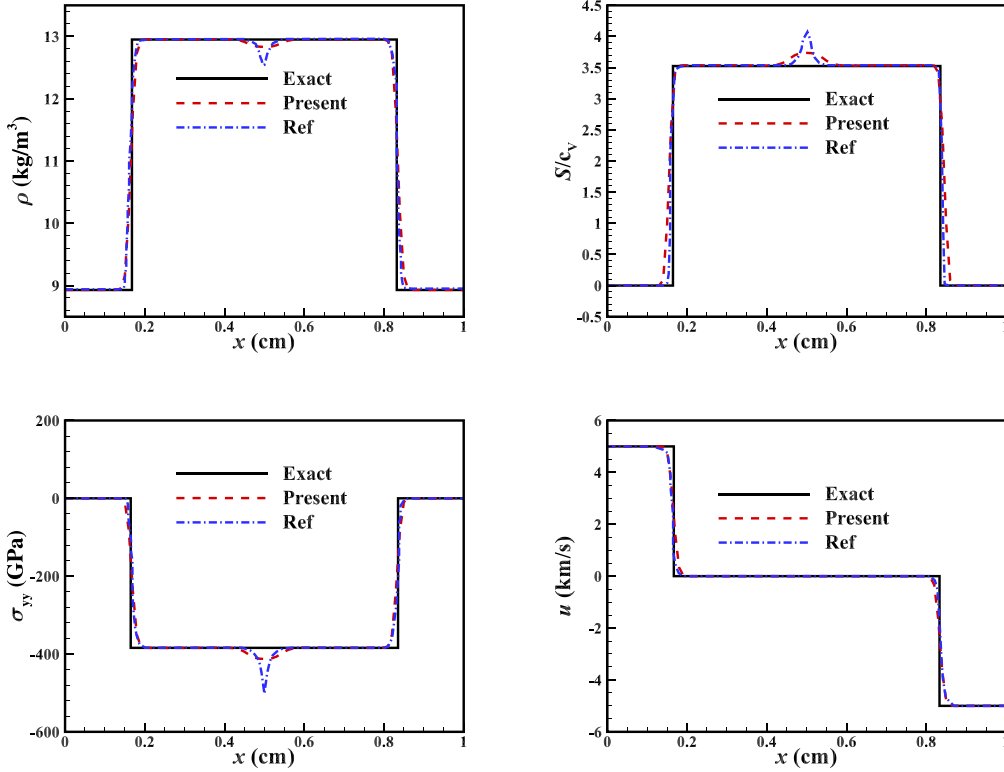


FIG. 2. Comparison of variables along the  $x$  direction at  $t = 0.3 \mu\text{s}$  obtained via our code (red dashed line) and those given in Ref. [37] (blue dash-dotted line) and those from the exact solution in Ref. [31] (black solid line).

0 km/s. With this setup, one of the shocks originated in the vertical colliding boundary ( $x = x_1$  cm) between the two different coppers travels to the right and exits the computational domain, while the other moves left towards I1. Note here that the interfaces I1 and I2 that are quantitatively examined remain in the computational domain during the whole simulation. A numerical sponge layer [36], which absorbs outgoing waves and minimizes reflection, is applied at the right boundary in the region  $x \in (7.2, 8)$  cm, as shown in the shaded part of Fig. 1. The left boundary does not need to be set because the material considered in area 3 is vacuum. The upper and lower boundaries are set to be periodic.

### B. Code validation

A detailed test study has been performed to further validate the code used based on the following two cases. The first test case is performed according to Ref. [31], in which two plates of unstressed elastic copper are impacted at  $x = 0.5$  cm with velocity  $u_L = (5, 0, 0)$  km/s for the left one and  $u_R = (-5, 0, 0)$  km/s for the right one. The parameters of the copper plates are set the same as those used in the present work. In Fig. 2, some representative results, such as the density  $\rho$ ,  $x$ -velocity  $u$ , stress component  $\sigma_{yy}$ , and the entropy  $S$ , are plotted along the  $x$  direction at  $t = 0.3 \mu\text{s}$  to compare with those given in Ref. [37]. It is seen that a fairly good agreement is achieved, although deviations at  $x = 0.5$  are observed for different variables due to the overheating effect, which is also present in previous numerical simulations [31,37] while absent in the analytical theory [31].

The second test case is a prototypic case of multi-interface elastic-plastic RMI described above which, however, has a flat solid-vacuum interface ( $\xi_0 = 0$ ). According to the previous work by Liu *et al.* [26], it is assured that the present numerical method using a grid resolution of  $\Delta x = \Delta y = 0.025$  cm is reliable to simulate the elastic-plastic solid-vacuum RMI in our work. The perfect plastic model of the two coppers with the same yield stress of 0.5 GPa, which is the same as that used by Dimonte *et al.* [19] and Liu *et al.* [26], is considered in this test. Some representative results, including the initial left-travelling plastic shock wave velocity  $U_s$ , the jump in normal velocity  $\Delta u$  across the shock, the long-term yield copper density  $\rho_Y$ , and the interface velocity  $V_0$ , are compared in Table II with those obtained by Dimonte *et al.* [19] and Liu *et al.* [26]. It is shown that the present simulation obtains results that agree fairly well with those of Dimonte *et al.* [19], confirming that the program can be extended from the solid-vacuum RMI problem [26] to the elastic-plastic RMI problem of multiple interfaces considered in our present study.

TABLE II. Comparison between the results obtained by the present simulation and that of Dimonte *et al.* [19] and Liu *et al.* [26].

	Dimonte's result	Liu's result	Present result	Units
$U_s$	7.64	7.87	7.86	km/s
$\Delta u$	5	5	5	km/s
$\rho_Y$	8.3	8.2	8.1	g/cm <sup>3</sup>
$V_0$	5.26	5.19	5.17	km/s

IV. RESULT AND DISCUSSIONS

A. Deformation mode

In the simulations of the solid-vacuum RMI problem, Liu *et al.* [26] systematically examined the solid-vacuum RMI at different initial perturbed interface amplitudes and yield stresses. They found that the interface deformation mode changes from the stable mode to the broken mode with the gradual increase of  $k\xi_0$  from 0.18 to 0.22 and the yield stress of 0.5 GPa fixed for coppers. Inspired by our previous findings, we turn to study the multi-interface elastic-plastic RMI problem in the present work, with research interest directed to examine the initial thickness of the copper layer ( $x = x_1$  cm) and the yield stress of the copper block ( $\sigma_{Y2}$ ). According to Liu *et al.* [26], the simulations are performed with the initial amplitude ( $k\xi_0$ ) of I1 and the yield stress of the copper layer ( $\sigma_{Y1}$ ) fixed at (0.2, 0.5 GPa). The typical modes of the interface deformation, which have been identified as the broken mode and the stable mode in Ref. [26], have also been found in the present simulations. As reported in our previous work [26], the oscillatory mode occurs in the case with large yield stress of material ( $\sigma_Y \geq 4$  GPa) and the main reason is that the material near the interface changes quickly from the plastic state induced by the initial shock to the elastic states due to the large yield stress. As the yield stress of the copper layer  $\sigma_{Y1}$  is fixed at 0.5 GPa, the oscillatory mode is absent, with the initial thickness of the copper layer and the yield stress of the copper block ( $x_1, \sigma_{Y2}$ ) varying from (0.5 cm, 1.0 GPa) to (1.0 cm, 6.0 GPa) according to the present simulations. Possibly, it may occur in the cases with other parameter settings, which should be explored as one of the motivations in our future work.

At the early stage of interface deformation for these two modes, the observed interfacial behaviors, i.e., phase reversal and formation of bubble and spike, are basically the same as the classical heavy-light fluidlike RMI problem [38]. However, the long-term interfacial behaviors are different. For the broken mode, the spike finally separates from I1 as a result of the continuous increase of the I1 width ( $x_{w1} = x_{b1} - x_{s1}$ , where  $x_{b1}$  and  $x_{s1}$  are the  $x$  positions of the bubble and spike tips of I1, respectively), as shown in Fig. 3(a). For the stable mode, the spike and bubble of I1 grow to saturation and then the shape of I1 remains almost unchanged, characterized by the interface width of I1 maintaining a nearly constant positive value, as shown in Fig. 3(b).

Unlike the sharp-pointed spike in Refs. [39,40], the spike is found to be bulged [see Fig. 3(b)] during the formation of the spike of the two modes in the present simulations. The bulging phenomenon has been found in the numerical simulations [3,19] and the experiments [4,21]. It is originated in the elastic-plastic effect, which takes a role during the spike evolution so that the material of the spike experiences a switch between the elastic and plastic states. As a consequence, the bulge happens when the  $x$ -velocity of the spike tip does not always obtain the maximum value which, however, occurs in a small region immediately behind the spike tip, in that the spike tip will be bulged rather than continue to be sharp pointed.

Figure 4 shows the phase map of the interface deformation modes of I1 at different settings of ( $x_1, \sigma_{Y2}$ ). For a small thickness of the copper layer,  $x_1 \leq 0.6$  cm, the interface

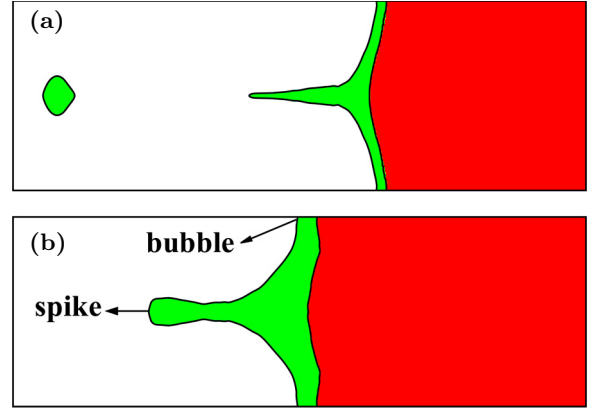


FIG. 3. Visualization of (a) the broken mode with the initial setting ( $x_1, \sigma_{Y2}$ ) = (0.5 cm, 4 GPa) and (b) the stable mode with the initial setting ( $x_1, \sigma_{Y2}$ ) = (1.0 cm, 4 GPa) of interface deformation at  $t = 200 \mu s$ . The green pattern represents material 1 and the red pattern represents material 2.

deformation is realized as the broken mode for all the yield stresses considered in our simulations, identified by a final separation of the spike resulting from the continuous increase in the width  $x_{w1}$  of the growing interface I1. For a larger thickness of the copper layer,  $x_1 \geq 0.8$  cm, the interface deformation is realized as the stable mode after a long-term interface growth of I1 for all the yield stresses in our simulations. For the copper layer whose initial thickness is between the two typical values, such as  $x_1 = 0.7$  cm, the interface deformation mode changes from the broken mode to the stable mode with the increase of yield stress ( $\sigma_{Y2}$ ) of the copper block. Moreover, for the case with initial setting ( $x_1, \sigma_{Y2}$ ) = (0.7 cm, 4 GPa), the broken mode transitions to the stable mode either by increasing the initial thickness of the copper layer or by increasing the yield stress of the copper block.

In the following, the interface deformation modes of I1 are closely scrutinized by four typical simulations of two groups

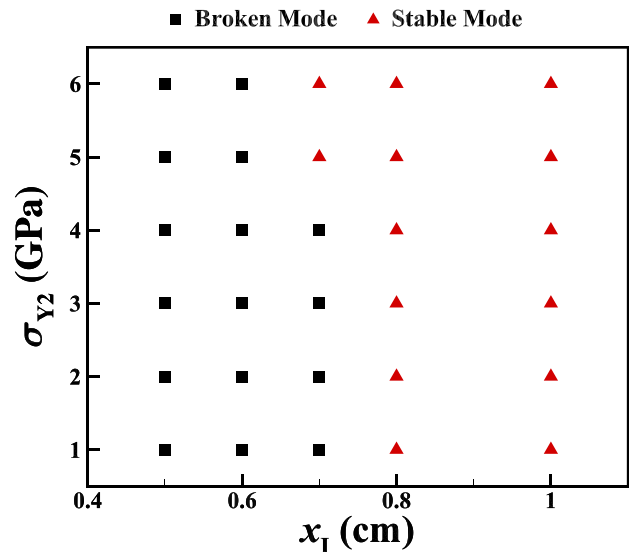


FIG. 4. Phase map of the interface deformation modes for different ( $x_1, \sigma_{Y2}$ ).

TABLE III. Parameter settings of  $(x_1, \sigma_{Y2})$  for four typical simulations.

Case	$x_1/\text{cm}$	$\sigma_{Y2}/\text{GPa}$	Deformation mode
A1	0.7	1.0	Broken mode
A2	0.7	6.0	Stable mode
B1	0.5	4.0	Broken mode
B2	1.0	4.0	Stable mode

either at a fixed  $x_1$  and varying  $\sigma_{Y2}$  or at a fixed  $\sigma_{Y2}$  and varying  $x_1$ , for which the parameter settings of  $(x_1, \sigma_{Y2})$  are listed in Table III as cases A1, A2, B1, and B2. The essential differences between the broken mode and the stable mode are illustrated, with a special interest focused on the wave motion at the early stage and the subsequent interface deformation, and quantitatively examined via the temporal variations of interface positions and velocities.

**B. Wave motion**

This section is mainly devoted to examine the wave motion of four typical cases of two deformation modes at different initial thickness of the copper layer and the yield stress of the copper block, i.e., cases A1, A2, B1, and B2, based on the numerical schlieren images visualized below. The numerical schlieren function  $\phi$  is calculated by Ref. [41],

$$\phi = \exp\left(-\frac{|\nabla\rho|}{\max|\nabla\rho|}\right), \tag{7}$$

where  $\nabla\rho$  is the density gradient. For all simulated cases, time  $t$  is set to be zero when the initial shocks are produced at the colliding interface.

For the broken mode case of group A, the wave motion at the early stage is demonstrated in Fig. 5. Specifically, Fig. 5(a) shows the initial shape of the copper layer which is between the interface 1 (I1) and the interface 2 (I2). I1 is the interface determining the deformation mode of the case and I2 is the interface at which the initial shocks (IS) are produced. Figure 5(b) shows the produced initial shocks,

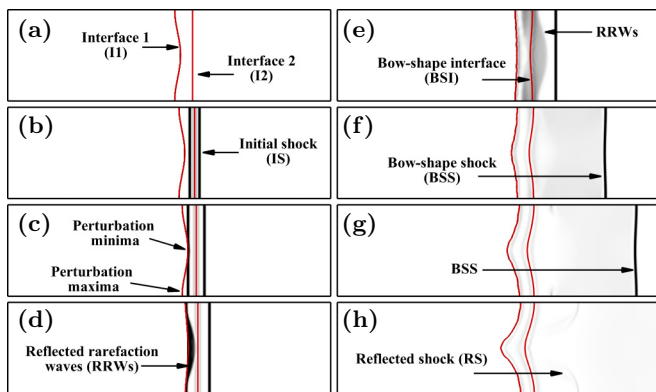


FIG. 5. Numerical schlieren images of wave motion for the broken mode (case A1) at  $t =$  (a) 0  $\mu\text{s}$ , (b) 0.4  $\mu\text{s}$ , (c) 0.7  $\mu\text{s}$ , (d) 1  $\mu\text{s}$ , (e) 2  $\mu\text{s}$ , (f) 5  $\mu\text{s}$ , (g) 7  $\mu\text{s}$ , (h) 10  $\mu\text{s}$ . The red lines represent the interfaces.

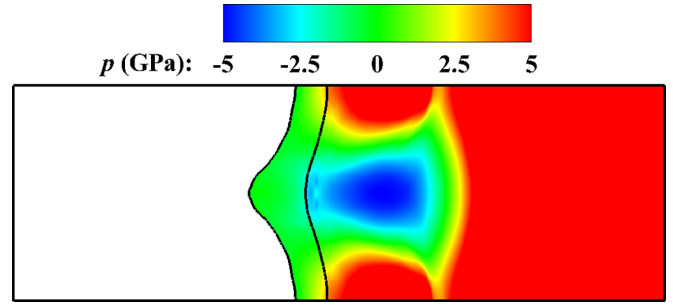


FIG. 6. Pressure contour plot at  $t = 10 \mu\text{s}$  of the broken mode (case A1).

resulting from the impact of the copper block at the copper layer, which are unstressed while with a relative velocity of 5 km/s. When the left-travelling IS impacts the perturbed interface I1 [see Fig. 5(c)], it first releases to zero pressure at the perturbation minima and then reflects back into the copper layer as a rarefaction wave. A short time later, IS releases to zero pressure at the perturbation maxima, also reflecting back into the copper layer as a rarefaction wave and at mean time there develops the reflected rarefaction waves (RRWs) in Fig. 5(d). Under these conditions, the stresses produced by IS interacting with the perturbed interface I1 cause I1 to experience the typical phase reversal of heavy-light RMI configurations in Figs. 5(d)–5(f). Meanwhile, the RRWs slow down the I2 since it travels across I2 due to the decrease of pressure, i.e., first in the middle, then the top and bottom of I2 due to the convex head of the RRWs. As a result, the planar I2 changes to be a bow-shaped interface (BSI) in Fig. 5(e). The RRWs subsequently travel to the right to catch up the strong initial shock from behind and slow down the shock, also first in the middle, then the top and bottom due to the convex shape of RRWs. Consequently, the initial shock changes to be a bow-shaped shock (BSS) in Fig. 5(f). According to the discussion in Ref. [26], due to the growth of I1 and I2 in the whole simulation, the material behind the bubble of the I2 is compressed and the material behind the spike of I2 is in tension. As evidence, Fig. 6 shows the hydrostatic pressure ( $p$ ) contour at  $t = 10 \mu\text{s}$ . Here,  $p$  is calculated from the stress ten-

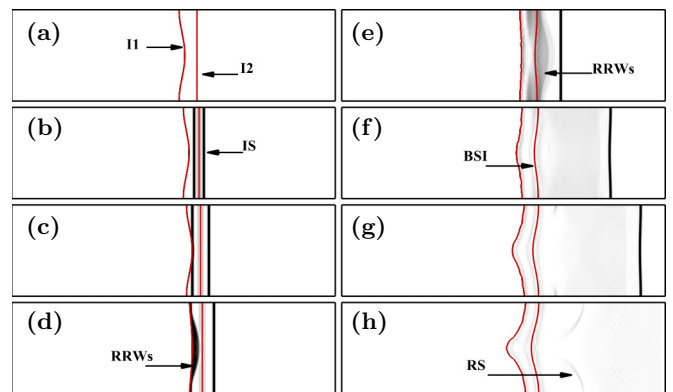


FIG. 7. Numerical schlieren images of wave motion for the stable mode (case A2) at  $t =$  (a) 0  $\mu\text{s}$ , (b) 0.4  $\mu\text{s}$ , (c) 0.7  $\mu\text{s}$ , (d) 1  $\mu\text{s}$ , (e) 2  $\mu\text{s}$ , (f) 5  $\mu\text{s}$ , (g) 7  $\mu\text{s}$ , (h) 10  $\mu\text{s}$ . The red lines represent the interfaces.

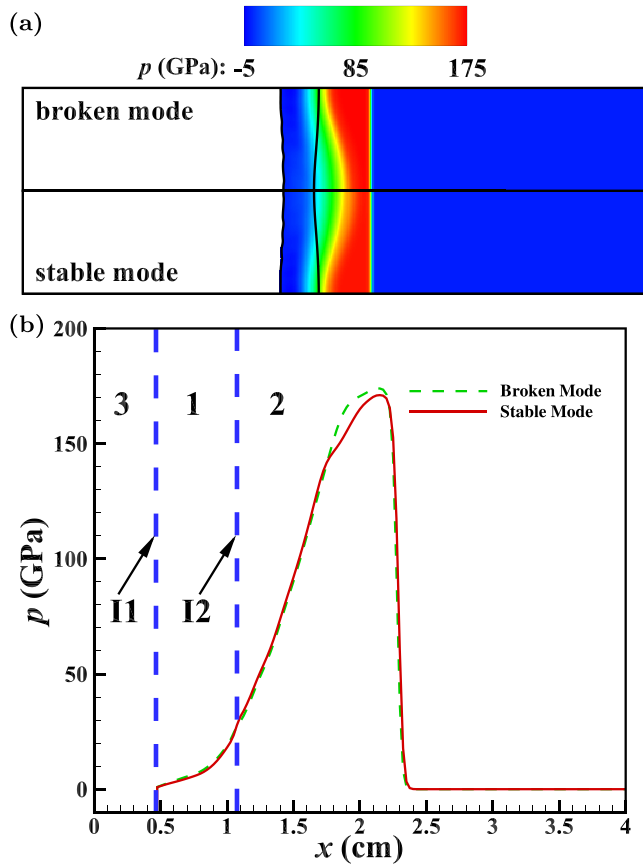


FIG. 8. Pressure comparison of the above two modes at  $t = 2 \mu\text{s}$ . (a) The pressure contour of the whole domain in which the pressure contour of the broken mode (case A1) is shown in the upper half and that of the stable mode (case A2) is shown in the lower half. (b) The pressure along the  $x$  direction ( $y = 2.15 \text{ cm}$ ) of the two modes.

sor  $\sigma$ ,  $p = -(\sigma_{xx} + \sigma_{yy} + \sigma_{zz})/3$ , whose negative or positive values correspond to isotropic tension or compression state of the material. It is obviously seen that the material behind the bubble of the I2 is compressed with the positive pressure and the material behind the spike of the I2 is in tension with the negative pressure. Within that, the reflected shock (RS) is developed to offset the pressure difference between these two areas, as shown in Fig. 5(h).

For the stable mode realized by increasing the yield stress of the copper block to  $\sigma_{Y2} = 6.0 \text{ GPa}$  and fixing the initial thickness of copper layer  $x_1 = 0.7 \text{ cm}$ , the wave motion behaves basically similar to that of the broken mode described above, although a little difference exists as discussed below. Specifically, Figs. 7(a)–7(f) demonstrate similar wave motions involving in sequence the formation of IS, the impacting of the IS at the perturbed interface I1, the subsequent formation of RRWs, and the resulting phase reversal and the deformation from I2 to BSI. After the RRWs travel across the I2, the RRWs become weaker than that of the broken mode (case A1), as shown in Fig. 7(e). Furthermore, the RRWs also become invisible and the RS appears in a similar manner, as shown in Figs. 7(f)–7(h).

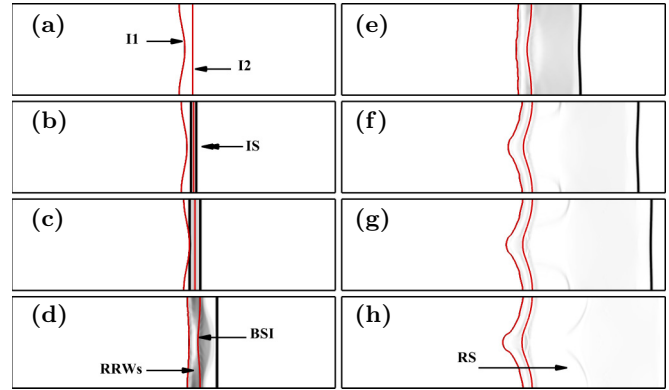


FIG. 9. Numerical schlieren images of wave motion for the broken mode (case B1) at  $t^* =$  (a)  $-0.44 \mu\text{s}$ , (b)  $-0.2 \mu\text{s}$ , (c)  $0 \mu\text{s}$ , (d)  $1 \mu\text{s}$ , (e)  $3 \mu\text{s}$ , (f)  $7 \mu\text{s}$ , (g)  $8 \mu\text{s}$ , (h)  $10 \mu\text{s}$ . The red lines represent the interfaces.

As a close examination, the strengths of the RRWs of these two modes at  $t = 2 \mu\text{s}$  are compared by the contour of the hydrostatic pressure ( $p$ ) plotted in Fig. 8. Since the problem solution has an up-and-down symmetry, the pressure contour of the broken mode is plotted in the upper half in Fig. 8(a), and that of the stable mode is plotted in the lower half to obtain a clear comparison. Figure 8(b) shows the comparison of the pressure along the  $x$  direction ( $y = 2.15 \text{ cm}$ ) of the two modes. The two vertical blue dashed lines represent the  $x$  positions of the interfaces at  $y = 2.15 \text{ cm}$  and the areas 1, 2, and 3 represent the copper layer, copper block, and vacuum, respectively. Clearly, for the broken mode case in which the yield stress of the copper block  $\sigma_{Y2} = 1.0 \text{ GPa}$  is smaller compared to that of the stable mode case, the pressure behind I2 is larger so that the spike of I2 gains a negative velocity of larger magnitude. This larger velocity of the spike of I2 results in the larger width of I1 after the continuous increase and the separation of the spike from I1. The detailed discussion is given in Sec. IV C.

Before the discussion of the wave motion for the two deformation modes of group B, the time  $t^*$ , which is set to

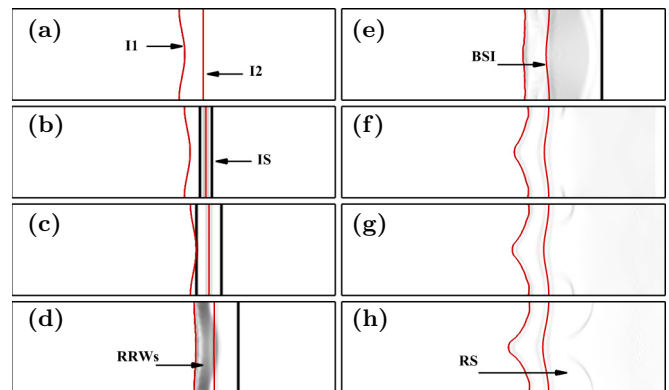


FIG. 10. Numerical schlieren images of wave motion for the stable mode (case B2) at  $t^* =$  (a)  $-1.07 \mu\text{s}$ , (b)  $-0.5 \mu\text{s}$ , (c)  $0 \mu\text{s}$ , (d)  $1 \mu\text{s}$ , (e)  $3 \mu\text{s}$ , (f)  $7 \mu\text{s}$ , (g)  $8 \mu\text{s}$ , (h)  $10 \mu\text{s}$ . The red lines represent the interfaces.

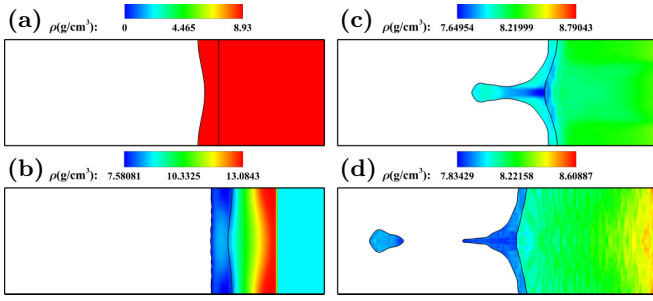


FIG. 11. Density contour plots for the broken mode (case A1) at  $t =$  (a)  $0 \mu\text{s}$ , (b)  $3 \mu\text{s}$ , (c)  $50 \mu\text{s}$ , (d)  $200 \mu\text{s}$ . The black lines represent the interfaces.

be zero corresponding to the moment when the IS impacts the I1, is used to get a clear comparison of the two modes with different initial thicknesses of the copper layer. For the two modes of group B, the wave motion behaves basically similar to that of the broken mode of group A described above, although a little difference exists when compared with

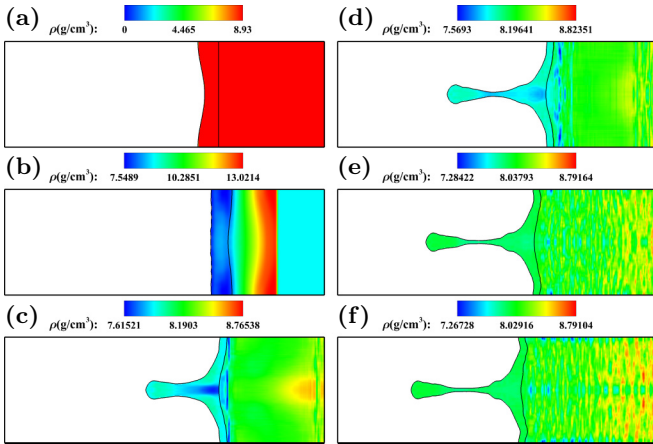


FIG. 12. Density contour plots for the stable mode (case A2) at  $t =$  (a)  $0 \mu\text{s}$ , (b)  $3 \mu\text{s}$ , (c)  $50 \mu\text{s}$ , (d)  $100 \mu\text{s}$ , (e)  $150 \mu\text{s}$ , (f)  $200 \mu\text{s}$ . The black lines represent the interfaces.

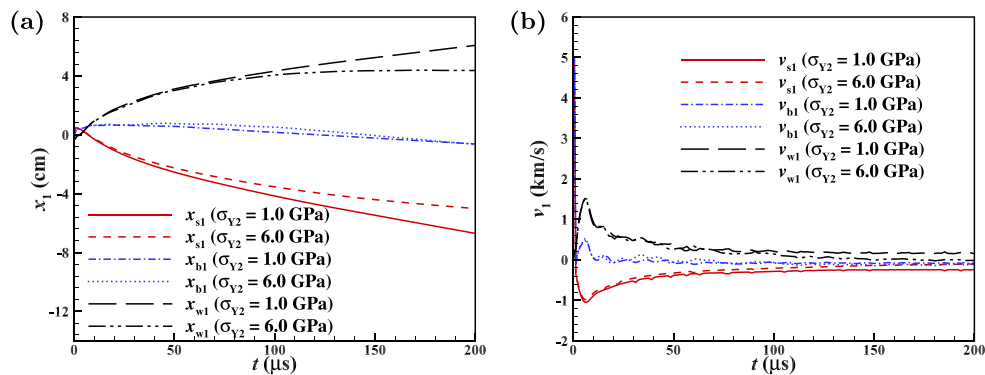


FIG. 13. Time evolution of (a) the  $x$  position of the spike tip ( $x_{s1}$ ), the bubble tip ( $x_{b1}$ ), and the interface width ( $x_{w1}$ ), and (b) the  $x$ -velocity of the spike tip ( $v_{s1}$ ), the bubble tip ( $v_{b1}$ ), and the interface width growth rate ( $v_{w1}$ ) of I1 for the two modes (cases A1 and A2).

each other. Specifically, Figs. 9(a)–9(c) and Figs. 10(a)–10(c) demonstrate, in sequence, the initial shape of the copper layer with different initial thickness, the formation of IS, and the impacting of the IS at the perturbed I1. Figures 9(c)–9(e) and Figs. 10(c)–10(e) both show the the subsequent formation of the RRWs, the resulting phase reversal, and the deformation from I2 to the BSI, but the position and the strength of the RRWs are different at the same time. At the time  $t^* = 0 \mu\text{s}$  of the two modes, the RRWs develop in the copper layer as a solution of the Riemann problem originated at I1. At  $t^* = 1 \mu\text{s}$ , the RRWs reach the I2 in the stable case [see Fig. 10(d)], while those of the broken mode have traveled across the I2 [see Fig. 9(d)], and thus the I2 is still planar in the stable mode while that of the broken mode has become a bow-shaped interface, causing the spike of I2 to gain a negative velocity with smaller magnitude. Correspondingly, the width of I1 in the stable mode case increases slower and it remains a constant value at the long term, rather than increasing continuously.

### C. Interface deformation

Next, our main focus is devoted to demonstrate the interface deformation of the two typical modes by four cases with different initial thicknesses of the copper layer and the yield stresses of the copper block, based on the visualization of density contours and the time evolution of the spike tip position, the bubble tip position, and the interface width of the two interfaces obtained by the simulation results.

Figure 11 depicts a sequence of density contour plots for the broken mode of group A, which is identified by a final separation of the spike from the perturbed I1. Specifically, the initial copper layer contains two interfaces, namely, the perturbed interface I1 between the vacuum and copper layer and the plane interface I2 between the copper layer and the copper block [see Fig. 11(a)]. After the impact of the IS originated in the vertical colliding boundary I2 between the copper layer and the copper block, the perturbed interface I1 experiences the phase reversal, i.e., the interface changes from being concave to being convex, as shown in Figs. 11(a) and 11(b). As the spike tip of I1 has a higher velocity than that of the bubble tip of I1, the perturbed interface I1 develops and transitions to a shape characterized by a long and thin

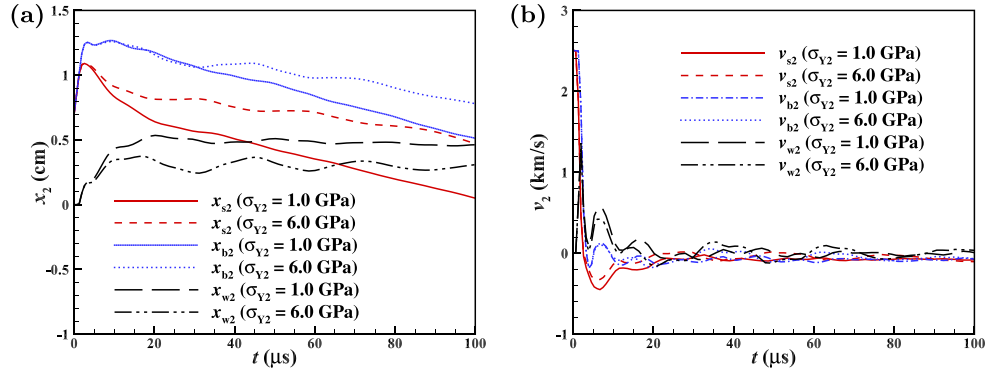


FIG. 14. Time evolution of (a) the  $x$  position of the spike tip ( $x_{s2}$ ), the bubble tip ( $x_{b2}$ ), the interface width ( $x_{w2}$ ), and (b) the  $x$ -velocity of the spike tip ( $v_{s2}$ ), the bubble tip ( $v_{b2}$ ), and the interface width growth rate ( $v_{w2}$ ) of I2 for the two modes (cases A1 and A2).

spike and commensurate bubbles [see Fig. 11(c)]. Finally, the interface width of I1 increases continuously and the spike eventually separates from I1 after a long-term evolution in Fig. 11(d).

The density contour plots for the stable mode (case A2) are shown in Fig. 12. Similar to the broken mode, the interface deformation also develops with the typical phase reversal and formation of spike and bubble, as demonstrated in Figs. 12(a)–12(c). In contrast, for the stable mode, the velocity of the spike tip of I1 decreases faster; thus the spike tip is soon at the same velocity as the bubble of I1. In the long term ( $t \geq 150 \mu\text{s}$ ), the spike and bubble tips obtain the same speed, so that the interface width of I1 grows to a saturated value in Fig. 12(e). Finally, the whole material moves at a nearly same velocity, namely, the moving interface maintains at the stable mode characterized by the interface shape remaining almost unchanged [see Figs. 12(e) and 12(f)].

In Fig. 13(a), the interface deformation of the two modes is quantitatively examined by the time evolution of the  $x$  position of the spike tip ( $x_{s1}$ ), the bubble tip ( $x_{b1}$ ), and the interface

width ( $x_{w1}$ ) of I1. Correspondingly, Fig. 13(b) shows the comparison of the  $x$ -velocity of the spike tip ( $v_{s1}$ ), the  $x$ -velocity of the bubble tip ( $v_{b1}$ ), and the interface width growth rate ( $v_{w1} = v_{b1} - v_{s1}$ ) of these two modes. For the broken mode in which the yield stress  $\sigma_{Y2} = 1.0 \text{ GPa}$ ,  $v_{s1}$  that is negative increases slowly at  $t \geq 10 \mu\text{s}$  and is smaller than  $v_{b1}$  all the time so that  $v_{w1}$  maintains a positive value [see Fig. 13(b)]. Hence,  $x_{w1}$  is continuously increasing, which leads to the final separation of the spike from I1. For the stable mode in which a larger yield stress  $\sigma_{Y2} = 6.0 \text{ GPa}$  is applied,  $v_{s1}$  increases faster than that of the broken mode [see Fig. 13(b)] and in the long term ( $t \geq 150 \mu\text{s}$ )  $v_{s1} \approx v_{b1}$ . Correspondingly,  $v_{w1}$  decreases gradually to be almost zero [see Fig. 13(b)] and the perturbed interface maintains a nearly constant positive  $x_{w1}$  in the long term [see Fig. 13(a)]. This is the characteristic of the stable mode.

The deformation of I2 of these two modes is also quantitatively examined by the time evolution of the  $x$  position of the spike tip ( $x_{s2}$ ), the bubble tip ( $x_{b2}$ ), and the interface width ( $x_{w2} = x_{b2} - x_{s2}$ ), as shown in Fig. 14(a). Figure 14(b) shows the comparison of the  $x$ -velocity of the spike tip ( $v_{s2}$ ), the  $x$ -velocity of the bubble tip ( $v_{b2}$ ), and the interface width growth rate ( $v_{w2} = v_{b2} - v_{s2}$ ) of the two modes, correspondingly. As discussed in Sec. IV B, with the decrease of the yield stress  $\sigma_{Y2}$  from 6.0 to 1.0 GPa, the RRWs across I2 become stronger (the pressure behind the spike tip of I2 is larger), so that the

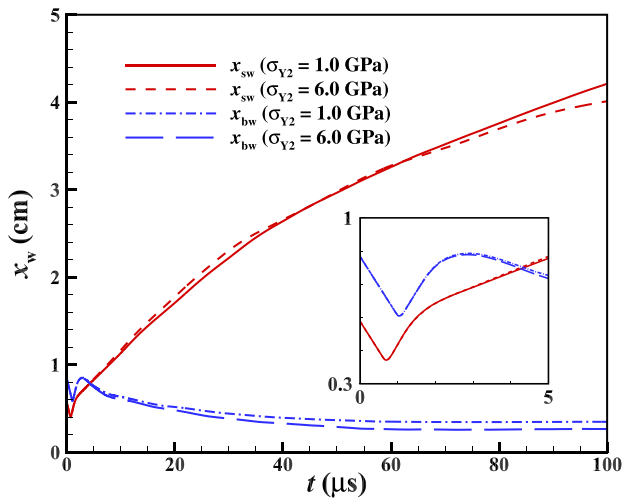


FIG. 15. Time evolution of the copper layer width between two spike tips ( $x_{sw}$ ) and bubbles ( $x_{bw}$ ) for the two modes (case A1 and case A2).

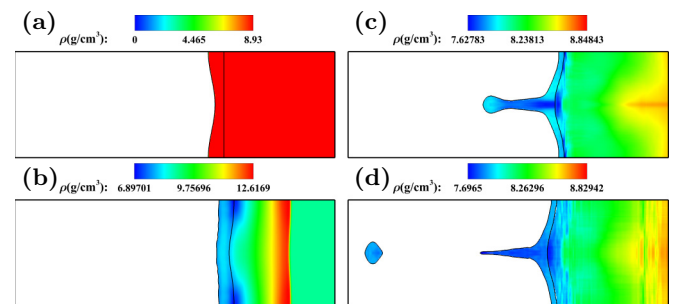


FIG. 16. Density contour plots for the broken mode (case B1) at  $t =$  (a)  $0 \mu\text{s}$ , (b)  $3.44 \mu\text{s}$ , (c)  $50 \mu\text{s}$ , (d)  $200 \mu\text{s}$ . The black lines represent the interfaces.

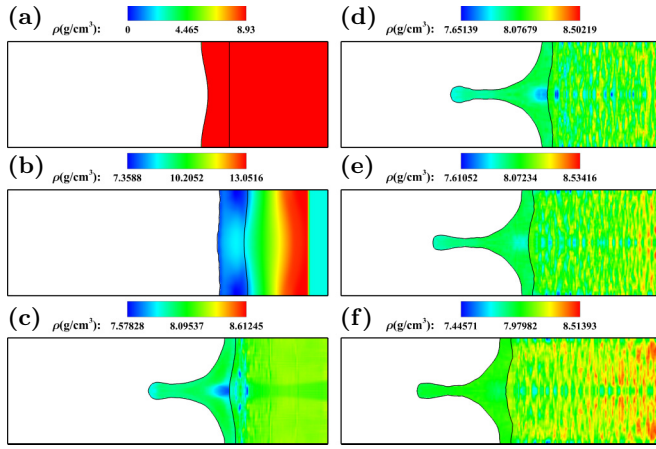


FIG. 17. Density contour plots for the stable mode (case B2) at  $t =$  (a) 0  $\mu\text{s}$ , (b) 3  $\mu\text{s}$ , (c) 50  $\mu\text{s}$ , (d) 100  $\mu\text{s}$ , (e) 150  $\mu\text{s}$ , (f) 200  $\mu\text{s}$ . The black lines represent the interfaces.

negative velocity of the spike tip of I2 has a larger magnitude at  $t \leq 20 \mu\text{s}$ , as shown in Fig. 14(b). Meanwhile, the velocities of the bubble tip of the two cases are nearly the same so that the growth rate of I2,  $v_{w2}$ , is larger than that of the case with the yield stress of 6.0 GPa. Correspondingly, the interface width of I2 increases faster for the case with smaller yield stress  $\sigma_{Y2} = 1.0$  GPa and reaches a larger maximum value, as shown in Fig. 14(a).

The time evolution of the copper layer width between two spike tips ( $x_{sw} = x_{s2} - x_{s1}$ ) and bubbles ( $x_{bw} = x_{b2} - x_{b1}$ ) for these two modes is compared in Fig. 15. As shown in the enlarged view, the time evolution of  $x_{sw}$  and  $x_{bw}$  for these two modes is nearly the same at  $t \leq 5 \mu\text{s}$ .  $x_{sw}$  decreases at first because of the initial velocity of I1. When the initial IS impacts the I1, the spike of I1 gains a negative velocity which increases  $x_{sw}$ . Finally,  $x_{sw}$  increases with a smaller velocity after the RRWs travel across the I2. Meanwhile, the width between the two bubble tips develops similar to that between the two spike tips. With the increase of yield stress of the copper block from 1.0 to 6.0 GPa, the growth rate of  $x_{sw}$  is larger since the negative velocity of the spike of I2 has a smaller magnitude after the RRWs travel across the I2, so that  $x_{sw}$  is larger than that of the case with yield stress of

1.0 GPa for the copper block since  $t \leq 45 \mu\text{s}$ , as shown in Fig. 15. Meanwhile, the width of the bubble is smaller than that of the case with 1.0 GPa. The smaller width of the case with yield stress of 1.0 GPa for the copper block represents smaller tension, so that the width of the spike tip increases faster to be a larger one at  $t \geq 45 \mu\text{s}$  than that of the case with 6.0 GPa yield stress for the copper block, as shown in Fig. 15. Finally, once the larger width of the spike tips reaches the critical value, the spike separates from I1, leading to a transition of the deformation mode from the stable mode to the broken mode.

Figures 16 and 17 depict the sequence of density contour plots for the broken mode and the stable mode of group B, respectively. The developments of the interface deformation of the two cases are similar to that described above. At the early stage, the typical phase reversal and formation of the spike and bubble of the interface deformation also appear in these cases, as shown in Figs. 16(a)–16(c) and Figs. 17(a)–17(c). For the broken mode, the interface width increases continuously since the negative velocity of the spike is larger than that of the bubble and the spike eventually separates from the interface after a long-term evolution in Fig. 16(d). For the stable mode, the whole interface moves at a nearly same velocity with no shape change of the interface, as shown in Figs. 17(d)–17(f).

Following the above discussion, the time  $t^*$  is also used here to replace  $t$  to get a clear comparison of the two cases with different initial thickness of the copper layer. Correspondingly,  $x^*$  which is set to be zero at  $t^* = 0$  is used to replace  $x$ . In Fig. 18(a), the interface deformations of these two modes are quantitatively examined by the time evolution of  $x_{s1}$ ,  $x_{b1}$ , and  $x_{w1}$ . Correspondingly, Fig. 18(b) shows the comparison of  $v_{s1}$ ,  $v_{b1}$ , and  $v_{w1}$  of these two modes. At the time  $t^* \leq 50 \mu\text{s}$ , the velocities of the spike tip  $v_{s1}$  and bubble tip  $v_{b1}$  are nearly the same in the two cases, as shown in Fig. 18(b). Correspondingly, the  $x$  positions of the spike tip  $x_{s1}$  and the bubble tip  $x_{b1}$  are nearly the same in the two cases, as shown in Fig. 18(a). Meanwhile, the negative velocity of the spike tip of the broken case slightly increases to have a larger magnitude than that of the stable case until  $50 \mu\text{s}$ . After  $t^* = 50 \mu\text{s}$ , the velocity of the spike is smaller than that of the bubble for all the time of the broken mode, while the velocity

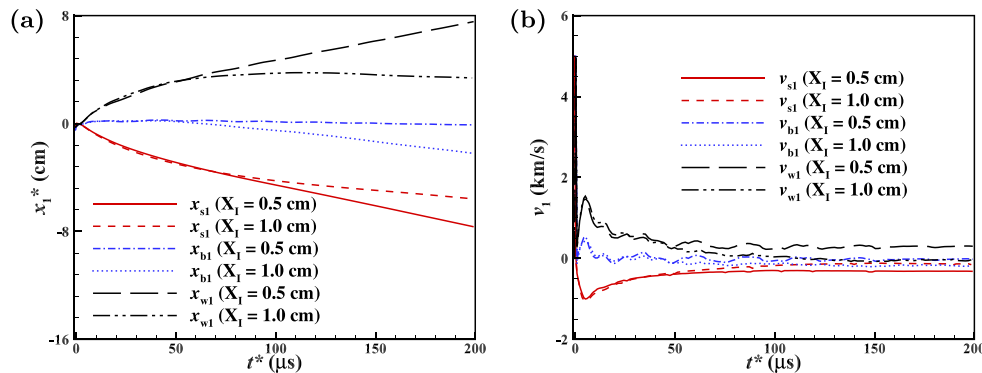


FIG. 18. Time evolution of (a) the  $x$  position of the spike tip ( $x_{s1}$ ), the bubble tip ( $x_{b1}$ ), and the interface width ( $x_{w1}$ ), and (b) the  $x$ -velocity of the spike tip ( $v_{s1}$ ), the bubble tip ( $v_{b1}$ ), and the width growth rate ( $v_{w1}$ ) of I1 for the two modes (case B1 and case B2).

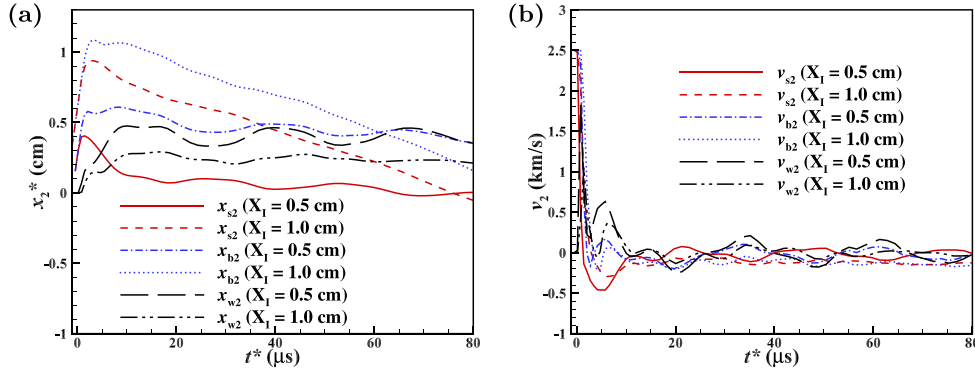


FIG. 19. Time evolution of (a) the  $x$  position of the spike tip ( $x_{s2}$ ), the bubble tip ( $x_{b2}$ ), and the interface width ( $x_{w2}$ ), and (b) the  $x$ -velocity of the spike tip ( $v_{s2}$ ), the bubble tip ( $v_{b2}$ ), and the width growth rate ( $v_{w2}$ ) of I2 for the two modes (case B1 and case B2).

of the spike increases to be the same as that of the bubble of the stable mode, as shown in Fig. 18(b). The interface width also increases continuously in the broken mode, while that in the stable mode remains nearly constant, as shown in Fig. 18(a).

The deformation of I2 is also quantitatively examined by the time evolution of positions  $x_{s2}$ ,  $x_{b2}$ , and  $x_{w2}$  shown in Fig. 19(a), along with the velocities  $v_{s2}$ ,  $v_{b2}$ , and  $v_{w2}$  shown in Fig. 19(b). As discussed in Sec. IV B, with the increase of the initial thickness of the copper layer from 0.5 to 1.0 cm, the RRWs impact I2 at a later moment with a commensurate weaker strength, so that the negative velocity of the spike tip of I2 has a smaller magnitude than that of the case with an initial thickness of 0.5 cm for the copper layer, as shown in Fig. 19(b). Meanwhile, the velocity of the bubble tip of I2 also has a smaller magnitude so that the growth rate of I2,  $v_{w2}$ , is smaller than that of the case with the initial thickness of 0.5 cm for the copper layer. Correspondingly, the interface width of I2 increases faster for the case with smaller initial thickness  $x_1 = 0.5$  cm and reaches a larger maximum value, as shown in Fig. 19(a).

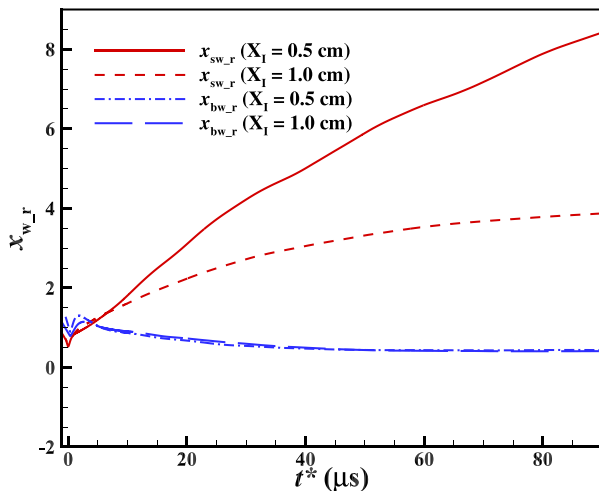


FIG. 20. Time evolution of the copper layer width between the two spike tips and bubbles for the two modes (cases B1 and B2).

Figure 20 shows the comparison of the widths between the two spike tips  $x_{sw}$  and bubbles  $x_{bw}$  for these two modes. The relative widths of the copper layer,  $x_{sw,r} = x_{sw}/x_1$  and  $x_{bw,r} = x_{bw}/x_1$ , representing the effect of compression or tension, are used to get a clear comparison of the two modes with different initial thickness ( $x_1$ ) of the copper layer. The result shows that even though the interface widths of I1 are nearly the same at  $t^* \leq 50 \mu\text{s}$  of the two cases [see Fig. 18(a)], the material located at the middle of the copper layer of the broken mode has been stretched larger than that of the stable mode. The difference in material stretch is mainly attributed to the deformation of I2 which results from the RRWs. The larger material stretch results in the final separation of the spike from I1.

#### D. Analysis of broken spike

Further, quantitative examination of the interface evolution of the broken mode is performed via comparing the time evolution of the copper layer width between two spike tips ( $x_{sw}$ ) for all the cases whose deformation mode is the broken mode, as shown in Fig. 21. The discontinuity of each case corresponds to that the spike separates from the I1 and then  $x_{sw}$  represents the  $x$ -direction width of the broken spike. As shown by the enlarged view of Fig. 21, at the early stage, the width of the spike first decreases because of the initial velocity of I1 until the initial IS impacting the I1. Then the spike of I1 gains a negative velocity, so that  $x_{sw}$  increases. Finally, the spike of I2 gains a negative velocity after the RRWs travel across the I2, thus  $x_{sw}$  still increases but with a smaller growth rate. For the cases with the same initial thickness of the copper layer, the growth of the spike width ( $x_{sw}$ ) is nearly the same. At the long time,  $x_{sw}$  grows continuously until the spike separates from the I1, which is the characteristic of a broken mode. As Fig. 21 shows, the maximum value of  $x_{sw}$ , which represents the value of the spike width at the broken time, is slightly different for the cases with the same initial thickness of the copper layer. This maximum value increases with the increase of the initial thickness  $x_1$ .

The rescaled value of the spike width,  $x_{rsw} = x_{sw}/x_{sw}(t=0) * x_1$ , is used in our simulations to show the close comparison of the spike width for the broken mode with different initial thicknesses. As shown in Fig. 22, the

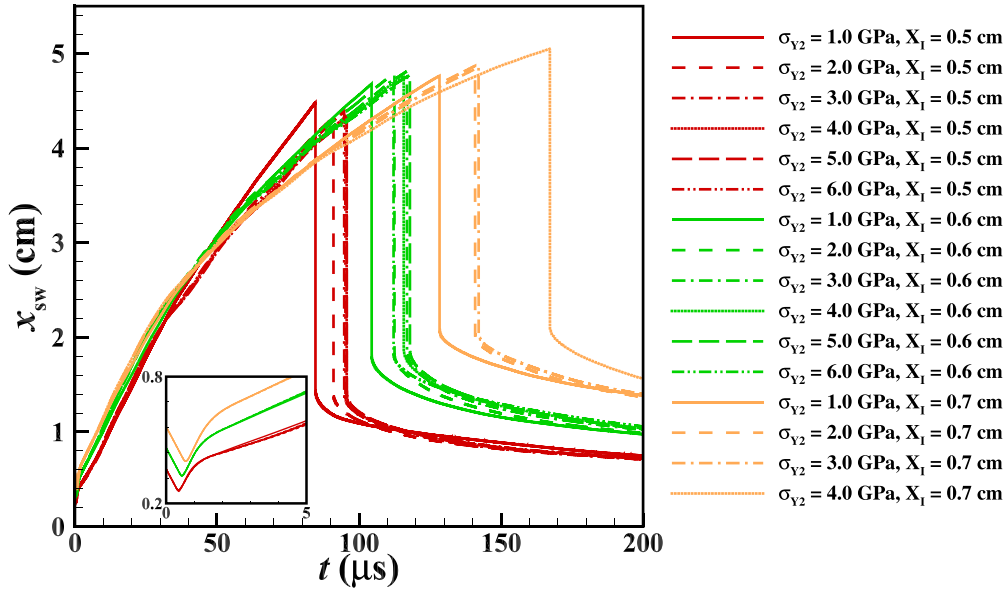


FIG. 21. Time evolution of the copper layer width between the two spikes ( $x_{sw}$ ) for the broken mode.

maximum value of the rescaled spike width,  $x_{rsw,m}$ , is about 6 cm for all the cases of the broken mode in our simulations. The yield stress of the copper block  $\sigma_{Y2}$  shows a slight influence on  $x_{rsw,m}$ . The maximum value of the rescaled spike width  $x_{rsw,m}$  can be regarded as the critical value at which the interface deformation is realized as the broken mode.

### V. CONCLUDING REMARKS

In this paper, we performed numerical simulation on the elastic-plastic RMI of multiple interfaces. This RMI problem is realized by a copper layer that is flanked by vacuum and a copper block of different material strength. The research efforts are directed to reveal the influence of layer thickness

and material strength on the deformation of the perturbed interface. Two typical modes of interface deformation are identified as the broken mode and the stable mode for different settings of the initial thickness ( $x_1$ ) of the copper layer and the yield stress ( $\sigma_{Y2}$ ) of the copper block. In particular, these modes are closely scrutinized by four typical simulations of two groups either at a fixed  $x_1$  and varying  $\sigma_{Y2}$  or at a fixed  $\sigma_{Y2}$  and varying  $x_1$ . The essential difference among these modes is illustrated, with special interest focused on the wave motion at the early stage and the subsequent interface deformation, and quantitatively examined via the temporal variations of interface positions and velocities.

At the early stage of interface deformation for the four cases, the observed wave motions and interfacial behaviors

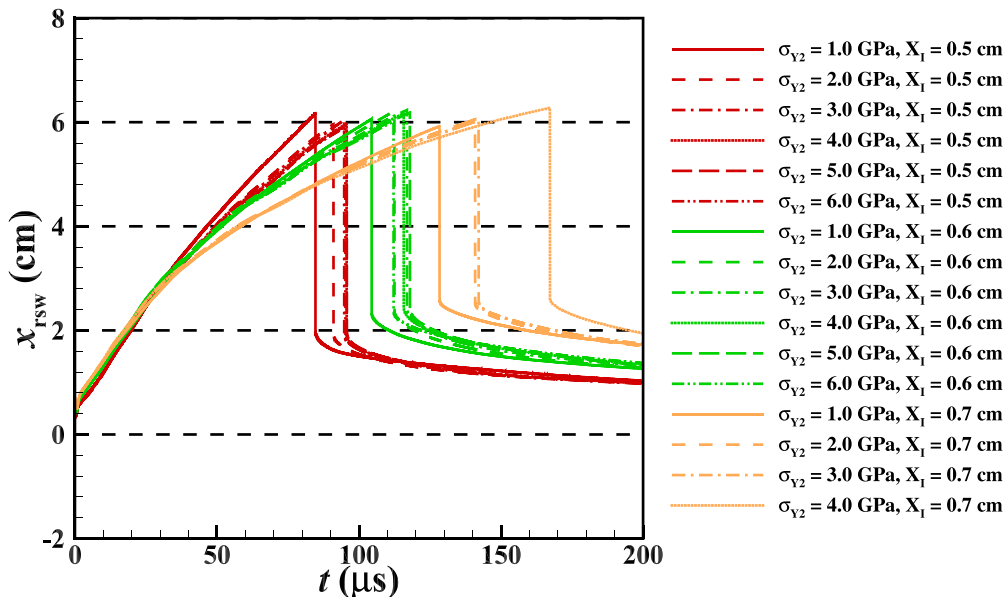


FIG. 22. Time evolution of the rescaled value of the spike width ( $x_{rsw}$ ).

are basically the same as the classical heavy-light fluidlike RMI problem. Specifically, the formation of IS, the impacting of IS at the perturbed interface I1, the subsequent formation of the RRWs, and the resulting phase reversal are nearly the same in all the typical cases. However, there also exists a difference of the typical cases, which results in different deformation modes. For the cases in which the initial thickness of the copper layer is fixed at  $x_1 = 0.7$  cm, with the decrease of the yield stress of the copper block  $\sigma_{Y2}$  from 6.0 to 1.0 GPa, the pressure behind the I2 becomes larger, resulting in a negative velocity with larger magnitude of the spike of I2. The negative velocity  $v_{s2}$  with a larger magnitude results in the smaller width of the spike width ( $x_{sw}$ ) and thus smaller tension. The smaller tension leads to a larger velocity of the spike of I1 ( $v_{s1}$ ) so that the width ( $x_{w1}$ ) of I1 becomes larger and the spike finally separates from I1. Hence, the interface deformation obtains a transition from the stable mode to the broken mode. For the cases that the yield stress of the copper block is fixed at  $\sigma_{Y2} = 4.0$  GPa, with the decrease of the initial thickness of the copper layer  $x_1$  from 1.0 to 0.5 cm, the RRWs travel across I2 faster and are larger at the same time, so that the spike of I2 gains a negative velocity with larger magnitude which results in a larger width of I1. Consequently,

the interface deformation changes from the stable mode to the broken mode.

Moreover, quantitative examination of the interface evolution of the broken mode is performed via comparing the time evolution of the width of two spike tips ( $x_{sw}$ ). The rescaled value of the spike width,  $x_{rsw} = x_{sw}/x_{sw}(t=0) * x_1$ , is used in our simulation to show the close comparison of the spike width for the broken mode with different initial thicknesses, and the result shows that the deformation mode changes from the stable mode to the broken mode since  $x_{rsw}$  reaches a critical value  $x_{rsw,c} = 6.0$  cm.

#### ACKNOWLEDGMENTS

This work is supported by the National Natural Science Foundation of China (Grants No. 12172353, No. 92052301, No. 11621202, No. 12202436, and No. 12388101), the Science Challenge Project, and the National Science Foundation (Grant No. CBET0755269). The numerical calculations in this paper have been done on the supercomputing system in the Supercomputing Center of University of Science and Technology of China.

- 
- [1] R. D. Richtmyer, Taylor instability in shock acceleration of compressible fluids, *Comm. Pure Appl. Math.* **13**, 297 (1960).
  - [2] E. E. Meshkov, Instability of the interface of two gases accelerated by a shock wave, *Fluid Dyn.* **4**, 101 (1972).
  - [3] A. López Ortega, M. Lombardini, D. I. Pullin, and D. I. Meiron, Numerical simulations of the Richtmyer-Meshkov instability in solid-vacuum interfaces using calibrated plasticity laws, *Phys. Rev. E* **89**, 033018 (2014).
  - [4] W. T. Buttler, D. M. Oró, D. L. Preston, K. O. Mikaelian, F. J. Cherne, R. S. Hixson, F. G. Mariani, C. Morris, J. B. Stone, G. Terrones, and D. Tupa, Unstable Richtmyer–Meshkov growth of solid and liquid metals in vacuum, *J. Fluid Mech.* **703**, 60 (2012).
  - [5] Lord Rayleigh, Investigation of the character of the equilibrium of an incompressible heavy fluid of variable density, *Proc. London Math. Soc.* **s1-14**, 170 (1882).
  - [6] G. I. Taylor, The instability of liquid surfaces when accelerated in a direction perpendicular to their planes. I, *Proc. R. Soc. London A* **201**, 192 (1950).
  - [7] J. D. Lindl, P. Amendt, R. L. Berger, S. G. Glendinning, S. H. Glenzer, S. W. Haan, R. L. Kauffman, O. L. Landen, and L. J. Suter, The physics basis for ignition using indirect-drive targets on the national ignition facility, *Phys. Plasmas* **11**, 339 (2004).
  - [8] J. Guzman and T. Plewa, Nonspherical core-collapse supernovae: Evolution towards homologous expansion, *Nonlinearity* **22**, 2775 (2009).
  - [9] M. Brouillette, The Richtmyer-Meshkov instability, *Annu. Rev. Fluid Mech.* **34**, 445 (2002).
  - [10] Y. Zhou, Rayleigh-Taylor and Richtmyer-Meshkov instability induced flow, turbulence, and mixing. I, *Phys. Rep.* **720**, 1 (2017).
  - [11] Y. Zhou, Rayleigh-Taylor and Richtmyer-Meshkov instability induced flow, turbulence, and mixing. II, *Phys. Rep.* **723**, 1 (2017).
  - [12] K. O. Mikaelian, Numerical simulations of Richtmyer-Meshkov instabilities in finite-thickness fluid layers, *Phys. Fluids* **8**, 1269 (1996).
  - [13] S. K. Shankar and S. K. Lele, Numerical investigation of turbulence in reshocked Richtmyer-Meshkov unstable curtain of dense gas, *Shock Waves* **24**, 79 (2014).
  - [14] Y. Liang, L. L. Liu, Z. G. Zhai, T. Si, and C.-Y. Wen, Evolution of shock-accelerated heavy gas layer, *J. Fluid Mech.* **886**, A7 (2020).
  - [15] M. Yuan, Z. Zhao, L. Liu, P. Wang, N.-S. Liu, and X.-Y. Lu, Instability evolution of a shock-accelerated thin heavy fluid layer in cylindrical geometry, *J. Fluid Mech.* **969**, A6 (2023).
  - [16] A. R. Piriz, J. J. López Cela, N. A. Tahir, and D. H. H. Hoffmann, Richtmyer-Meshkov flow in elastic solids, *Phys. Rev. E* **74**, 037301 (2006).
  - [17] J. N. Plohr and B. J. Plohr, Linearized analysis of Richtmyer-Meshkov flow for elastic materials, *J. Fluid Mech.* **537**, 55 (2005).
  - [18] A. R. Piriz, J. J. López Cela, N. A. Tahir, and D. H. H. Hoffmann, Richtmyer-Meshkov instability in elastic-plastic media, *Phys. Rev. E* **78**, 056401 (2008).
  - [19] G. Dimonte, G. Terrones, F. J. Cherne, T. C. Germann, V. Dupont, K. Kadau, W. T. Buttler, D. M. Oro, C. Morris, and D. L. Preston, Use of the Richtmyer-Meshkov instability to infer yield stress at high-energy densities, *Phys. Rev. Lett.* **107**, 264502 (2011).
  - [20] K. J. Frutsky and R. J. Clifton, High-temperature pressure-shear plate impact experiments on OFHC copper, *J. Mech. Phys. Solids* **46**, 1723 (1998).

- [21] B. J. Jensen, F. J. Cherne, M. B. Prime, K. Fezzaa, A. J. Iverson, C. A. Carlson, J. D. Yeager, K. J. Ramos, D. E. Hooks, J. C. Cooley, and G. Dimonte, Jet formation in cerium metal to examine material strength, *J. Appl. Phys.* **118**, 195903 (2015).
- [22] M. B. Prime, D. E. Vaughan, D. L. Preston, W. T. Buttler, S. R. Chen, D. M. Oró, and C. Pack, Using growth and arrest of Richtmyer-Meshkov instabilities and Lagrangian simulations to study high-rate material strength, *J. Phys.: Conf. Ser.* **500**, 112051 (2014).
- [23] M. B. Prime, W. T. Buttler, M. A. Buechler, N. A. Denissen, M. A. Kenamond, F. G. Mariam, J. I. Martinez, D. M. Oró, D. W. Schmidt, J. B. Stone, D. Tupa, and W. Vogann-McNeil, Estimation of metal strength at very high rates using free-surface Richtmyer-Meshkov instabilities, *J. Dyn. Behav. Mater.* **3**, 189 (2017).
- [24] M. B. Prime, W. T. Buttler, S. J. Fensin, D. R. Jones, J. L. Brown, R. S. King, R. Manzanares, D. T. Martinez, J. I. Martinez, J. R. Payton, and D. W. Schmidt, Tantalum strength at extreme strain rates from impact-driven Richtmyer-Meshkov instabilities, *Phys. Rev. E* **100**, 053002 (2019).
- [25] M. B. Prime, A. Arsenlis, R. A. Austin, N. R. Barton, C. C. Battaile, J. L. Brown, L. Burakovsky, W. T. Buttler, S.-R. Chen, D. M. Dattelbaum, S. J. Fensin, D. G. Flicker, G. T. Gray, C. Greeff, D. R. Jones, J. M. D. Lane, H. Lim, D. J. Luscher, T. R. Mattsson, J. M. McNaney, H. S. Park, P. D. Powell, S. T. Prisbrey, B. A. Remington, R. E. Rudd, S. K. Sjue, and D. C. Swift, A broad study of tantalum strength from ambient to extreme conditions, *Acta Mater.* **231**, 117875 (2022).
- [26] X. Y. Liu, Z. Y. Zhao, N. S. Liu, and X. Y. Lu, Numerical simulations of the Richtmyer-Meshkov instability of solid-vacuum interface, *Adv. Appl. Math. Mech.* **15**, 1166 (2022).
- [27] P. T. Barton, D. Drikakis, and E. I. Romenski, An Eulerian finite-volume scheme for large elastoplastic deformations in solids, *Intl. J. Numer. Methods Eng.* **81**, 453 (2010).
- [28] P. T. Barton, R. Deiterding, D. Meiron, and D. Pullin, Eulerian adaptive finite-difference method for high-velocity impact and penetration problems, *J. Comput. Phys.* **240**, 76 (2013).
- [29] S. K. Godunov and E. I. Romenskii, Nonstationary equations of nonlinear elasticity theory in Eulerian coordinates, *J. Appl. Mech. Tech. Phys.* **13**, 868 (1972).
- [30] S. K. Godunov and E. Romenskii, *Elements of Continuum Mechanics and Conservation Laws* (Kluwer Academic/Plenum Publishers, New York, 2003).
- [31] V. A. Titarev, E. Romenski, and E. F. Toro, MUSTA-type upwind fluxes for nonlinear elasticity, *Intl. J. Numer. Methods Eng.* **73**, 897 (2008).
- [32] G.-S. Jiang and C.-W. Shu, Efficient implementation of weighted ENO schemes, *J. Comput. Phys.* **126**, 202 (1996).
- [33] C.-W. Shu and S. Osher, Efficient implementation of essentially non-oscillatory shock-capturing schemes, *J. Comput. Phys.* **77**, 439 (1988).
- [34] T. G. Liu, B. C. Khoo, and K. S. Yeo, Ghost fluid method for strong shock impacting on material interface, *J. Comput. Phys.* **190**, 651 (2003).
- [35] A. L. Ortega, M. Lombardini, D. I. Pullin, and D. I. Meiron, Numerical simulation of elastic-plastic solid mechanics using an Eulerian stretch tensor approach and HLLD Riemann solver, *J. Comput. Phys.* **257**, 414 (2014).
- [36] A. Subramaniam, N. S. Ghaisas, and S. K. Lele, High-order Eulerian simulations of multimaterial elastic-plastic flow, *J. Fluids Eng.* **140**, 050904 (2018).
- [37] G. Kluth and B. Després, Discretization of hyperelasticity on unstructured mesh with a cell-centered Lagrangian scheme, *J. Comput. Phys.* **229**, 9092 (2010).
- [38] G. Jourdan and L. Houas, High-amplitude single-mode perturbation evolution at the Richtmyer-Meshkov instability, *Phys. Rev. Lett.* **95**, 204502 (2005).
- [39] S. M. Bakhrah, I. Yu. Bezrukova, A. D. Kovaleva, S. S. Kosarim, and O. V. Ol'khov, On possible availability of the cumulative effect under shock loading of the curved surface of condensed matter, *AIP Conf. Proc.* **849**, 317 (2006).
- [40] A. M. Saunders, C. V. Stan, K. K. Mackay, B. Morgan, J. A. K. Horwitz, S. J. Ali, H. G. Rinderknecht, T. Haxhimali, Y. Ping, F. Najjar, J. Eggert, and H.-S. Park, Experimental observations of laser-driven tin ejecta microjet interactions, *Phys. Rev. Lett.* **127**, 155002 (2021).
- [41] A. Marquina and P. Mulet, A flux-split algorithm applied to conservative models for multicomponent compressible flows, *J. Comput. Phys.* **185**, 120 (2003).